crystals

MDPI

Article

Tuning the Electronic Properties of a Nitro- and Cyano-Functionalized Benzothienoquinolizinium Salt as Potential Organic N-Type Semiconductor: Experimental and Theoretical Study

Andrés Aracena [1,2,*], Kerry Wrighton-Araneda [3,4], Katherine Pezet [5], Diego Vilches [6], Felipe A. Angel [6,7,8], Ihan Chandía [1], César Zúñiga [1,2], Sebastián Elgueta [9] and Javiera González [1]

1 Facultad de Medicina Veterinaria y Agronomia, Instituto de Ciencias Naturales, Universidad de Las Americas, Sede Santiago (Campus Providencia), Avenida Manuel Montt 948, Providencia 7500000, Chile; ihan.chandia@gmail.com (I.C.); czuniga@udla.cl (C.Z.); javiera.gonzalez.vasquez2@edu.udla.cl (J.G.)
2 Centro de Investigacion en Ciencias Biologicas y Quimicas, Universidad de Las Americas, Avenida Manuel Montt 948, Providencia 7500000, Chile
3 Escuela de Kinesiología, Facultad de Ciencias de la Salud, Universidad Bernardo OHiggins, Santiago 8320000, Chile; kerry.wrighton@ubo.cl
4 Centro Integrativo de Biología y Química Aplicada (CIBQA), Universidad Bernardo OHiggins, Santiago 8320000, Chile
5 Departamento de Química, Facultad de Ciencias Naturales, Matemáticas y Medio Ambiente, Universidad Tecnológica Metropolitana (UTEM), J. P. Alessandri 1242, Ñuñoa 7800002, Chile; katherine.pezeta@utem.cl
6 Departamento de Química Inorgánica, Escuela de Química, Facultad de Química y de Farmacia, Pontificia Universidad Católica de Chile, Santiago 7820436, Chile; dpvilches@uc.cl (D.V.); faangel@uc.cl (F.A.A.)
7 Centro de Nanotecnología y Materiales Avanzados, CIEN-UC, Pontificia Universidad Católica de Chile, Santiago 7820436, Chile
8 Centro de Energía, CE-UC, Pontificia Universidad Católica de Chile, Santiago 7820436, Chile
9 Escuela de Nutricion y Dietetica, Facultad de Ciencias de la Rehabilitacion y Calidad de Vida, Universidad San Sebastian, Providencia 7500000, Chile; sebastian.elgueta@uss.cl
* Correspondence: aaracena@udla.cl

Abstract

A new nitro- and cyano-functionalized, tetradecyl-substituted benzothienoquinolizinium tetrafluoroborate was synthesized through oxidative photocyclisation of a pyridinium precursor and evaluated as a potential small molecule N-type organic semiconductor. The precursor and the photocyclised salts were characterized by UV–Vis absorption spectroscopy, DSC, ^{1}H and ^{13}C NMR, and cyclic voltammetry. Their optoelectronic properties were further investigated by DFT and TD-DFT calculations. Photocyclisation induced a marked bathochromic extension of the absorption profile, decreasing the optical band gap from 3.19 eV for the pyridinium precursor to 2.61 eV for the fused benzothienoquinolizinium salt. Cyclic voltammetry revealed a stabilized electrochemical LUMO level of approximately −3.87 eV, supporting the electron-deficient character of the nitro/cyano-substituted cationic scaffold. Frontier molecular orbital analysis showed that the HOMO and LUMO are mainly localized on the fused π-conjugated core and electron-withdrawing aryl substituents, with negligible contribution from the tetradecyl chain and BF_4^- counterion. TD-DFT and electron excitation analyses indicated that the monomeric low-energy transition has mixed local/charge-transfer character, whereas π-stacked dimers, especially the face-to-face arrangement, enhance charge transfer character and reduce electron–hole Coulombic attraction. Marcus type charge transport calculations revealed packing dependent behavior, with the face-to-face dimer displaying nearly ambipolar transport with a slight electron preference. A preliminary theoretical donor–acceptor model with hexaphenyl-substituted hexabenzocoronene further suggested energetic compatibility and strong intermolecular

Check for updates

Academic Editor: Anelia Kakanakova

Received: 18 July 2026
Revised: 21 August 2026
Accepted: 30 August 2026
Published: 2 September 2026

Copyright: © 2026 by the authors. Licensee MDPI, Basel, Switzerland. This article is an open access article distributed under the terms and conditions of the Creative Commons Attribution (CC BY) license.

charge-transfer character. Overall, these results identify this benzothienoquinolizinium tetrafluoroborate as a promising electron-deficient cationic π-scaffold for future organic optoelectronic materials.

Keywords: organic electronics; organic N-type semiconductors; non-fullerene acceptors

1. Introduction

Organic semiconductors have attracted sustained interest for applications in optoelectronic devices, including organic photovoltaics, light-emitting diodes, sensors, field-effect transistors, and photoactive molecular materials [1,2]. Their appeal arises from their structural tunability, solution processability, compatibility with flexible substrates, and the possibility of controlling optical and electronic properties through molecular design [2,3]. In organic photovoltaic systems, efficient device operation depends on the combination of P-type donor [4,5] and N-type acceptor materials [6], where the acceptor must display suitable electron affinity, adequate frontier orbital alignment, visible-light absorption, and favorable charge-transport characteristics [7,8]. Fullerene derivatives have historically been the most widely used N-type acceptors because of their high electron affinity and efficient electron transport [6]. However, their limited absorption in the visible region, restricted structural tunability, and stability-related limitations have motivated the development of non-fullerene acceptors based on organic small molecules [9]. Small-molecule acceptors are particularly attractive because their molecular structures can be modified in a predictable way to tune the HOMO/LUMO energy levels, optical band gaps, molecular packing, and charge-transport properties [10]. Therefore, the design of new electron-deficient π-conjugated scaffolds remains an important strategy for expanding the family of potential N-type organic semiconductors.

Polycyclic aromatic and heteroaromatic systems are promising platforms for this purpose due to their extended π-surfaces, which can favor intermolecular π–π interactions and supramolecular organization [11]. The incorporation of heteroatoms into fused aromatic frameworks provides an additional tool to modulate the electronic structure, redox response, optical absorption, and semiconductor character of these materials [12,13]. Moreover, molecular rigidity and planarity can improve electronic delocalization and promote organized packing, both of which are relevant for charge migration in the solid state [11–15]. Discotic and fused aromatic systems are especially interesting because columnar or lamellar arrangements can provide preferential pathways for charge transport [16,17].

Within this family, positively charged polycyclic aromatic hydrocarbons (PCPAHs) and cationic heteroaromatic systems represent an attractive but still comparatively underexplored class of electron-deficient π-materials. The presence of a positively charged nitrogen atom embedded in or connected to the aromatic framework increases the electron-accepting character of the molecule, while the extended π-system can support optical absorption and supramolecular assembly [18–23]. Previous studies have shown that cationic discotic PAHs can self-assemble into nanofibers, nanotubes, ribbons, two-dimensional nanostructures, and columnar organizations depending on the alkyl substituent, counterion, and ionic environment [18–23]. These features suggest that charged fused aromatic scaffolds can combine molecular electron deficiency with structural organization, two properties that are highly desirable for optoelectronic materials [24].

Pyridinium and quinolizinium derivatives are particularly relevant in this context because the quaternary nitrogen atom acts as a strong electron-withdrawing center. These cationic heteroaromatic units have been widely explored as acceptor fragments in donor–

acceptor chromophores, nonlinear optical materials, photoactive systems, and dye-related applications [25–27]. Extended quinolizinium-fused corannulene derivatives illustrate how the incorporation of a positively charged, electron-deficient heteroaromatic unit into a curved π-system can modulate its electronic structure [28]. In these systems, the quinolizinium fragment contributes to the stabilization of low-lying frontier molecular orbitals, particularly the LUMO, while π-extension, structural fusion, and molecular curvature influence the absorption profile and optical energy gap.

A useful synthetic route toward rigid cationic fused heteroaromatic systems is the oxidative photocyclisation of aryl-substituted pyridinium salts. Classical studies have demonstrated that 1,2-diaryl- and 1,2,6-triarylpyridinium cations can undergo photoinduced cyclisation or bicyclisation through excited-state processes followed by oxidative dehydrogenation, affording fused tetra- and polycyclic cationic frameworks [29,30]. Subsequent investigations of expanded pyridiniums confirmed that pericondensation strongly modifies the optical and photophysical properties of these compounds, extending their absorption into the visible region and increasing molecular rigidity [22]. These studies provide an important conceptual foundation for using photocyclisation as a strategy to transform flexible pyridinium precursors into planarized, electron-deficient π-conjugated cations.

Photobicyclised, tetradecyl-substituted benzodithienoquinolizinium salts have recently been proposed as potential non-fullerene organic N-type semiconductors based on their UV–Vis absorption, electrochemical LUMO levels, energy band gaps (HOMO-LUMO), and theoretical charge-transport analysis [31]. In particular, the tetradecyl-substituted derivative has shown promising theoretical electron-transport features, suggesting that this cationic fused scaffold could serve as a platform for further molecular engineering. In parallel, aggregation studies of related photocyclised pyridinium salts showed evidence of J-aggregate formation in water, supporting the ability of these planar cationic systems to organize through π-stacking interactions [32]. Theoretical studies of pyridinium stacking also indicate that aromatic cations can form π–π stacked structures under appropriate conditions, with substituent and solvent effects influencing the strength of these interactions [33].

Despite these advances, the electronic modulation of benzothienoquinolizinium-type scaffolds via strong electron-withdrawing substituents remains underexplored. In modern non-fullerene acceptor chemistry, peripheral and end-group functionalization is a powerful strategy for tuning absorption, frontier orbital energies, molecular packing, and photovoltaic performance [34–37]. Nitro groups are particularly strong electron-withdrawing substituents and have been shown to deepen frontier orbital levels, reduce optical gaps, alter absorption profiles, and influence molecular packing in acceptor–donor–acceptor systems [38,39]. Cyano-containing acceptor motifs are also widely used in high-performance organic acceptors because of their ability to stabilize LUMO levels and reinforce electron-accepting character [40,41]. Therefore, the simultaneous incorporation of nitro and cyano groups into a photocyclised cationic scaffold offers a rational approach to strengthen its potential N-type character.

Based on this background, the present work reports the synthesis and experimental theoretical study of a nitro- and cyano-functionalized, tetradecyl-substituted benzothienoquinolizinium salt obtained by oxidative photocyclisation of its pyridinium precursor. The molecular design combines two complementary strategies: rigidification and π-extension through photocyclisation, and LUMO stabilization through the introduction of strong electron-withdrawing substituents. The precursor (**3**) and photocyclised salt (**4**) were characterized by UV–Vis spectroscopy, ^{1}H and ^{13}C-NMR, Differential Scanning Calorimetry and cyclic voltammetry, while the optoelectronic properties of photocyclised salt were further evaluated using DFT and TD-DFT calculations, electronic excitation analysis, and

charge-transport calculations [31,42–56]. The results are discussed in comparison with the previously reported, tetradecyl-substituted benzodithienoquinolizinium platform and with representative organic N-type acceptor materials [31], aiming to assess the potential of this new cationic fused π-system as a small-molecule organic semiconductor with N-type character.

2. Materials and Methods

2.1. Synthesis of the Nitro- and Cyano-Functionalized Benzothienoquinolizinium Salt

The compounds were synthesized according to the route discussed in Section 3.1. The chalcone intermediate, (E)-4-(3-(4-nitrophenyl)acryloyl)benzonitrile (**1**), was obtained by base-catalyzed condensation of 4-acetylbenzonitrile with 4-nitrobenzaldehyde in the presence of NaOH [57,58].

The pyrylium salt precursor, 2-(4-cyanophenyl)-4-(4-nitrophenyl)-6-(thiophen-2-yl)pyrylium tetrafluoroborate (**2**), was prepared following a reported procedure by condensation of compound **1** with 2-acetylthiophene in the presence of tetrafluoroboric acid diethyl ether complex ($HBF_4{\cdot}Et_2O$) [59].

The pyridinium salt precursor, 2-(4-cyanophenyl)-4-(4-nitrophenyl)-1-(4-tetradecylphenyl)-6-(thiophen-2-yl)pyridin-1-ium tetrafluoroborate (**3**), was synthesized by refluxing equimolar amounts of pyrylium salt **2** and 4-tetradecylaniline (0.37 mmol) in ethanol (20 mL) for 8 h. The resulting precipitate was filtered, washed with cold ethanol, and recrystallized from ethanol. 67% yield, mp = 140 °C (DSC onset). ^{1}H NMR (400 MHz, acetone-d6) 8.88 (s, 2H), 8.53 (dd, J = 22.0, 8.9 Hz, 4H), 7.87–7.80 (m, 7H), 7.55 (d, J = 8.4 Hz, 2H), 7.16 (d, J = 8.4 Hz, 2H), 2.58–2.51 (m, 2H, Ar–CH2), 1.55–1.45 (m, 2H), 1.38–1.20 (m, 22H), 0.92–0.84 (m, 3H) (Figure S1). ^{13}C NMR (101 MHz, $CDCl_3$) δ 156.16, 155.58, 149.61, 146.86, 140.17, 136.57, 135.79, 132.97, 130.73, 130.20, 129.57, 127.94, 125.47, 124.58, 117.55, 114.52, 35.33, 30.04, 29.77, 29.42, 29.05, 22.81, 14.24 (Figure S2).

The photocyclised pyridinium salt, 11-cyano-2-(4-nitrophenyl)-8-tetradecylthieno[2′,3′:1,2]quinolizino[3,4,5,6-def]phenanthridin-14-ium tetrafluoroborate ($BTQ(NO_2,CN)C_{14}H_{29}BF_4$ (**4**)), was obtained by oxidative photocyclisation of precursor **3**. A solution of compound **3** (0.5 mmol) in 50 mL of a hexane/ethanol mixture (5:1, *v*/*v*) was placed in a quartz flask and irradiated for 80 h under O_2 using a Luzchem photoreactor (model LZC-4V/LZC-4VB) (Luzchem Research, Inc., Ottawa, ON, Canada) equipped with 300 nm lamps. The precipitated photocyclised tetrafluoroborate was filtered and recrystallized from ethanol to afford the target benzothienoquinolizinium tetrafluoroborate as a dark orange solid. 73% yield, mp= 108 °C (DSC onset). ^{1}H NMR (400 MHz, acetone-d6) δ 8.86 (s, 1H), 8.55–8.48 (m, 2H), 7.80 (s, 6H), 7.55 (d, J = 8.0 Hz, 2H), 7.15 (d, J = 7.0 Hz, 2H), 2.58–2.50 (m, 2H, Ar–CH_2), 1.60–1.45 (m, 2H), 1.40–1.20 (m, 22H), 0.93–0.84 (m, 3H) (Figure S4). ^{13}C NMR (101 MHz, $CDCl_3$) δ 156.43, 137.44, 133.03, 131.90, 130.42, 128.81, 125.44, 118.42, 115.35, 36.18, 32.00, 31.62, 30.62, 30.33, 29.90, 23.66, 15.10 (Figure S5).

2.2. Physical and Spectroscopic Characterization

Differential scanning calorimetry (DSC) characterizations were performed under a nitrogen flow of 20 mL min^{-1}. Samples of approximately 2.2 mg for compound **3** and 2.1 mg for compound **4** were first held at 30 °C for 1 min and then heated from 30 to 400 °C at a heating rate of 10 °C min^{-1}. The melting temperatures were determined from the onset of the endothermic transitions (Figures S3 and S6 respectively) observed in the first heating scan.

The optical properties were determined by UV–Vis absorption spectroscopy using a BelPhotonics UV-M51 spectrophotometer (BEL Engineering srl, Monza, Italy) UV–Vis

characterizations were carried out in acetonitrile (CH_3CN) and dichloromethane (CH_2Cl_2) at room temperature using quartz cuvettes with a 1 cm optical path length.

Structural characterization was performed by ^1H and ^{13}C NMR spectroscopy using a Bruker 400 MHz spectrometer (Bruker Corporation, Billerica, MA, USA) ^1H NMR spectra were recorded at 400 MHz in acetone-d6, while ^{13}C NMR spectra were recorded at 101 MHz in $CDCl_3$. Chemical shifts (δ) are reported in ppm relative to the residual solvent signals, and coupling constants (*J*) are reported in Hz.

2.3. Electrochemical Characterization

Electrochemical characterization was performed by cyclic voltammetry (CV) using an Epsilon Eclipse potentiostat (BASi) (BASi Research Products, Inc., West Lafayette, IN, USA) with a standard three-electrode configuration consisting of a platinum disk working electrode (0.126 cm^2), a platinum wire counter electrode, and an Ag/AgCl reference electrode. Cyclic voltammetry experiments were performed in anhydrous acetonitrile using 0.1 M tetrabutylammonium hexafluorophosphate (Bu_4NPF_6) as the supporting electrolyte and an analyte concentration of 1.0×10^{-3} M. Prior to each characterization, the solutions were purged with nitrogen for 10 min to remove dissolved oxygen. Voltammograms were recorded at a scan rate of 50 mV s^{-1} within a potential window from −1.5 to +1.5 V. Ferrocene/ferrocenium (Fc/Fc^+) was used as an internal standard for potential calibration.

2.4. Computational Methods

All quantum chemical calculations were carried out using the Gaussian 16 software package (revision B.01) [60]. Gas phase geometry optimizations of the nitro- and cyano-functionalized, tetradecyl-substituted benzothienoquinolizinium tetrafluoroborate BTQ(NO_2,CN)$C_{14}H_{29}BF_4$ (**4**) were performed using the M06-2X functional in combination with the 6-311G(d) basis set. The M06-2X functional was selected because of its established performance for main-group thermochemistry, π-conjugated systems, and medium-range noncovalent interactions, which are relevant for the description of π-stacked organic semiconductor models.

The monomeric salt and two representative π-stacked dimeric models, namely face-to-face (FF) and face-to-tail (FT) arrangements, were modeled including explicit BF_4^- counterions in order to preserve electroneutrality and provide a more realistic representation of the tetrafluoroborate salts. Representative dimer geometries were selected from a preliminary conformational screening of the parent BTQ scaffold, in which different relative positions of the BF_4^- counterions were evaluated. The FF and FT π-stacked motifs were selected as representative arrangements based on previous structural studies of related positively charged fused pyridinium/PQP-type scaffolds, where cofacial head-to-head, tail-to-tail, layered, and columnar π-stacked organizations have been observed by X-ray diffraction or inferred from bulk/solution self-assembly studies [18,19,22]. The stability of each arrangement was assessed using BSSE-corrected interaction energies calculated by the counterpoise method, as reported in the Supporting Information.

The most stable FF and FT arrangements identified from this screening were FF-sym-b and FT-asym-a, with interaction energies of −205.92 and −202.24 kJ mol^{-1}, respectively (Table S1). These geometries were then used as starting structures for the nitro/cyano functionalized FF and FT dimers of compound **4**. After introducing the NO_2 and CN substituents, the corresponding dimers were fully reoptimized at the M06-2X/6-311G(d) level. Frequency calculations were performed at the same level of theory for the monomeric salt to verify that the optimized geometry corresponded to a true minimum on the potential energy surface.

Frontier molecular orbital energies and orbital distributions were obtained from single-point B3LYP/6-311G(d) calculations performed on the M06-2X/6-311G(d)-optimized geometries. Electronic excitation properties were calculated using time-dependent density functional theory (TD-DFT) at the B3LYP/6-311G(d) level. The electronic transitions and electron–hole distributions were analyzed using Multiwfn 3.8 [61].

To address the possible limitations of B3LYP for charge-transfer excited states and to evaluate solvent effects, additional TD-DFT single point calculations were performed at the CAM-B3LYP-D3/6-311G(d) level using the SMD continuum model for acetonitrile. These calculations were carried out on the previously optimized gas phase M06-2X geometries of the monomeric salt **4**, the FF and FT π-stacked dimers, and the HBC-PhC_{12}···**4** donor–acceptor complex. No geometry reoptimization was performed in solvent for this validation step. The CAM-B3LYP-D3/SMD(CH_3CN) calculations were used to assess the robustness of the qualitative excited-state assignments, particularly for transitions with charge-transfer character. Charge-transport descriptors for the FF and FT dimeric arrangements were calculated from the M06-2X/6-311G(d) optimized geometries within the Marcus theory framework.

For the donor–acceptor model, HBC-PhC_{12}, and the HBC-PhC_{12}···**4** complex were optimized in the gas phase at the M06-2X/6-31G(d,p) level. Single point B3LYP/6-311G(d) calculations were then performed on these optimized geometries to evaluate the frontier orbital alignment and donor–acceptor energetic compatibility. The electronic excitation associated with the HBC-PhC_{12}···**4** complex was analyzed using Multiwfn 3.8 [61]. Additional TD-CAM-B3LYP-D3/6-311G(d)/SMD(CH_3CN) calculations were also performed for this complex to verify whether the intermolecular charge-transfer character was preserved upon inclusion of long-range exchange and solvent polarization.

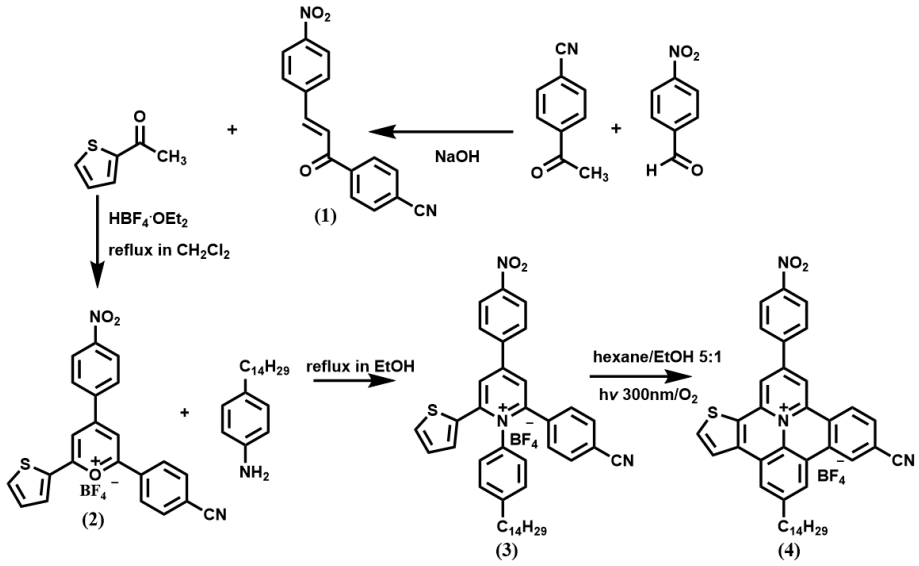
3. Results

3.1. Synthesis of the Polycyclic Heteroaromatic Salts

The synthetic route toward the nitro- and cyano-functionalized benzothienoquinolizinium tetrafluoroborate is shown in Scheme 1. The preparation of the target compound followed a stepwise strategy based on the construction of a suitably substituted pyridinium precursor and its subsequent oxidative photocyclisation to generate the fused cationic heteroaromatic scaffold [29,30]. The chalcone intermediate, (E)-4-(3-(4-nitrophenyl)acryloyl)benzonitrile (**1**), was obtained by base-catalyzed condensation of 4-acetylbenzonitrile with 4-nitrobenzaldehyde. Subsequent acid-mediated cyclization with 2-acetylthiophene in the presence of tetrafluoroboric acid diethyl ether complex afforded the corresponding pyrylium tetrafluoroborate, 2-(4-cyanophenyl)-4-(4-nitrophenyl)-6-(thiophen-2-yl)pyrylium tetrafluoroborate (**2**). This sequence provides the electron-deficient pyrylium platform bearing both cyano and nitro substituents, which are retained in the final photocyclised salt. Conversion of pyrylium salt **2** into the corresponding pyridinium precursor was achieved by reaction with 4-tetradecylaniline under reflux in ethanol. This transformation afforded 2-(4-cyanophenyl)-4-(4-nitrophenyl)-1-(4-tetradecylphenyl)-6-(thiophen-2-yl)pyridin-1-ium tetrafluoroborate (**3**). The introduction of the tetradecylphenyl group was intended to provide a hydrophobic side chain analogous to those previously used in related photobicyclised pyridinium-derived systems, where long alkyl substituents can influence solubility, processability, and potential supramolecular organization.

The final step consisted of oxidative photocyclisation of pyridinium precursor **3** under O_2 irradiation at 300 nm in a hexane/ethanol mixture (5:1, *v*/*v*). Under these conditions, the initially non-fused pyridinium salt (**3**) was converted into the planarized polycyclic cationic framework, affording 11-cyano-2-(4-nitrophenyl)-8-tetradecylthieno[2′,3′:1,2]quinolizino

[3,4,5,6-def]phenanthridin-14-ium tetrafluoroborate (BTQ(NO_2,CN)$C_{14}H_{29}BF_4$ (**4**)) as a dark-orange solid.



Scheme 1. Synthetic route toward the nitro- and cyano-functionalized, tetradecyl-substituted benzothienoquinolizinium tetrafluoroborate.

The successful formation of the photocyclised salt **4**, is relevant from a molecular-design perspective because the reaction converts a conformationally flexible pyridinium precursor into a more rigid and extended π-conjugated cationic scaffold. At the same time, the presence of cyano and nitro substituents is expected to reinforce the electron-accepting character of the system by stabilizing the LUMO level. Thus, compound **4** combines two complementary design elements: structural planarization through photocyclisation and electronic modulation through strong electron-withdrawing substituents [38–40].

3.2. Spectroscopic UV-Vis Characterization

The UV–Vis absorption spectra of the pyridinium salt precursor **3** and the photocyclised nitro- and cyano-functionalized, tetradecyl-substituted benzothienoquinolizinium tetrafluoroborate **4** were recorded in acetonitrile at room temperature (Figure 1) to ensure consistency with the electrochemical characterizations.

The non-fused pyridinium salt **3** shows an absorption onset at 389 nm, corresponding to an optical band gap of 3.19 eV. In contrast, the photocyclised salt **4** exhibits a red-shifted absorption onset at 475 nm, corresponding to a reduced optical band gap of 2.61 eV. The optical band gaps were estimated from the absorption edge according to Equation (1), following the same approach used for related benzodithienoquinolizinium tetrafluoroborates [31,62]:

$$E_{gopt} = 1240/\lambda \text{ onset} \quad (1)$$

where E_{gopt} is the optical band gap in eV and λ onset is the absorption onset wavelength in nm.

The bathochromic displacement of the absorption edge from 389 nm for precursor **3** to 475 nm for the photocyclised compound **4** corresponds to a decrease of approximately 0.58 eV in the optical band gap. This decrease is consistent with the structural transformation induced by oxidative photocyclisation, which converts the conformationally more flexible pyridinium precursor into a rigid, planarized, and more extended polycyclic cationic π-system. Such planarization increases effective conjugation and favors lower-energy

electronic transitions, as previously observed for related photocyclised pyridinium-derived heteroaromatic salts [31,32].

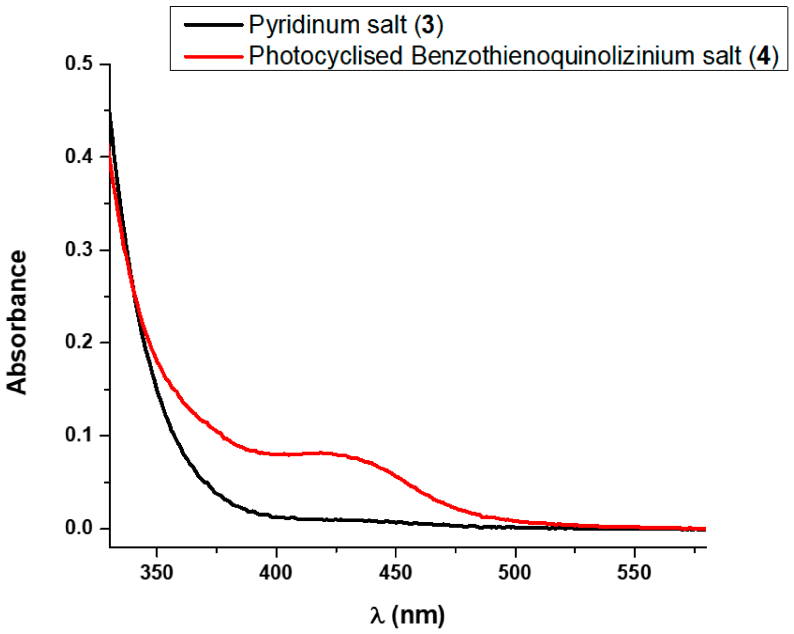


Figure 1. UV–Vis absorption spectra of the pyridinium precursor **3** (black) and the photocyclised benzothienoquinolizinium tetrafluoroborate **4** (red) in acetonitrile as solvent.

The broader absorption tail of compound **4** into the visible region is particularly relevant for optoelectronic applications, since visible-light absorption is a desirable feature for small-molecule acceptor materials. The reduced optical band gap of **4** also supports the hypothesis that the fused benzothienoquinolizinium framework, combined with strong electron-withdrawing substituents, promotes a more electron-deficient and optically active potential N-type material. The experimentally determined optical band gap of **4** will also be used in combination with electrochemical data to estimate the HOMO energy level from the electrochemical LUMO, following the strategy commonly applied to organic semiconductor candidates [63,64].

3.3. Electrochemical Studies

Cyclic voltammetry was used to evaluate the electron-accepting character of the pyridinium precursor **3** and the photocyclised benzothienoquinolizinium tetrafluoroborate **4**. The voltammetric profiles were recorded in anhydrous acetonitrile using Bu_4NPF_6 as supporting electrolyte, with ferrocene/ferrocenium (Fc/Fc^+) as an internal reference. The corresponding voltammograms, including those of the blank electrolyte and Fc/Fc^+ reference, are shown in the Supporting Information (Figures S7–S10). The experimental ferrocene half-wave potential was determined as 0.472 V vs. Ag/AgCl, allowing the reduction potentials of the compounds to be referenced to Fc/Fc^+. The electrochemical report gives reduction potentials of −0.466 V for **3** and −0.463 V for **4** vs. Ag/AgCl (Figures S5 and S6), together with the derived LUMO, optical gap, and HOMO values.

The LUMO energy levels were estimated from the reduction potentials using the conventional ferrocene-referenced relation [63,64]:

$$E_{LUMO} = -(E_{red} - E_{Fc/Fc+} + 4.80)\ eV \quad (2)$$

where E_{red} is the reduction potential determined versus Ag/AgCl, E_{Fc/Fc^+} is the half-wave potential of ferrocene versus Ag/AgCl, and 4.80 eV corresponds to the energy level of

Fc/Fc^+ below vacuum. When the reduction potential is already expressed versus Fc/Fc^+, Equation (2) can be written equivalently as:

$$E_{LUMO} = -(E_{red,vs\cdot Fc/Fc^+} + 4.80)\ eV \quad (3)$$

The HOMO energy levels were then estimated by combining the electrochemical LUMO values with the optical band gaps obtained from the UV–Vis absorption onsets:

$$E_{HOMO} = E_{LUMO} - E_{gopt} \quad (4)$$

The resulting electrochemical and optical parameters are summarized in Table 1.

Table 1. Electrochemical and optical parameters of the pyridinium precursor **3** and photocyclised benzothienoquinolizinium tetrafluoroborate **4** using acetonitrile as solvent.

Compound	E_{red} vs. Ag/AgCl/V	E_{LUMO}/eV	E_{gopt}/eV	E_{HOMO}/eV
3	−0.466	−3.86	3.19	−7.05
4	−0.463	−3.87	2.61	−6.48

The pyridinium precursor **3** and the photocyclised salt **4** display very similar reduction potentials, leading to nearly identical electrochemical LUMO levels of −3.86 eV and −3.87 eV, respectively. This indicates that the first reduction process is strongly governed by the electron-deficient cationic scaffold and by the presence of the nitro and cyano substituents. The small difference between both LUMO values suggests that photocyclisation does not substantially alter the thermodynamic accessibility of the first reduction under the present experimental conditions.

However, the optical and electronic consequences of photocyclisation become evident when the LUMO values are combined with the optical band gaps. Precursor **3** exhibits an estimated HOMO level of −7.05 eV, whereas photocyclised compound **4** shows a higher HOMO level of −6.48 eV. This change is consistent with the decrease in optical band gap from 3.19 eV to 2.61 eV, previously determined from the UV–Vis absorption onset. Therefore, the main electronic effect of photocyclisation is not a large additional LUMO stabilization between **3** and **4**, but rather a narrowing of the optical gap associated with rigidification and extension of the π-conjugated polycyclic system.

Importantly, the electrochemical LUMO value of compound **4** lies in the range expected for electron-accepting organic materials and is more stabilized than that previously reported for the analogous alkylated benzodithienoquinolizinium platforms [31]. In the related BPDTQ series, UV–Vis and voltammetric data were used to estimate LUMO levels and energy band gaps consistent with N-type semiconductor behavior, with the tetradecyl derivative identified as especially promising based on charge-transport calculations. In the present case, the incorporation of nitro and cyano groups shifts the electrochemical LUMO of the photocyclised scaffold to approximately −3.87 eV, placing it closer to the range of classical fullerene-type acceptors [65]. Although differences in the experimental conditions should be taken into account, this result is consistent with the stronger electron-withdrawing character introduced by the nitro and cyano substituents and supports the enhanced electron-accepting character of compound **4**.

3.4. Theoretical Studies

3.4.1. Frontier Molecular Orbitals of Compound **4**: Monomeric and π-Stacked Dimeric Models

The frontier molecular orbitals of the photocyclised benzothienoquinolizinium tetrafluoroborate **4** were analyzed for the monomeric salt and for two π-stacked dimeric models.

The geometries of the monomer and dimers, including explicit BF_4^- counterions, were optimized in the gas phase at the M06-2X/6-311G(d) level. Frontier molecular orbital energies were then estimated from single-point calculations at the B3LYP/6-311G(d) level on the optimized geometries.

The explicit inclusion of BF_4^- counterions provides a more realistic description of the isolated molecular salt compared with previous calculations on related benzodithienoquinolizinium systems, which were performed mainly on the isolated cationic species. In the present case, the frontier orbital distributions indicate that the BF_4^- counterions do not contribute significantly to either the HOMO or the LUMO (Figure 2). Therefore, their main role in these models is associated with charge compensation and ion-pair geometry rather than direct participation in the frontier electronic structure.

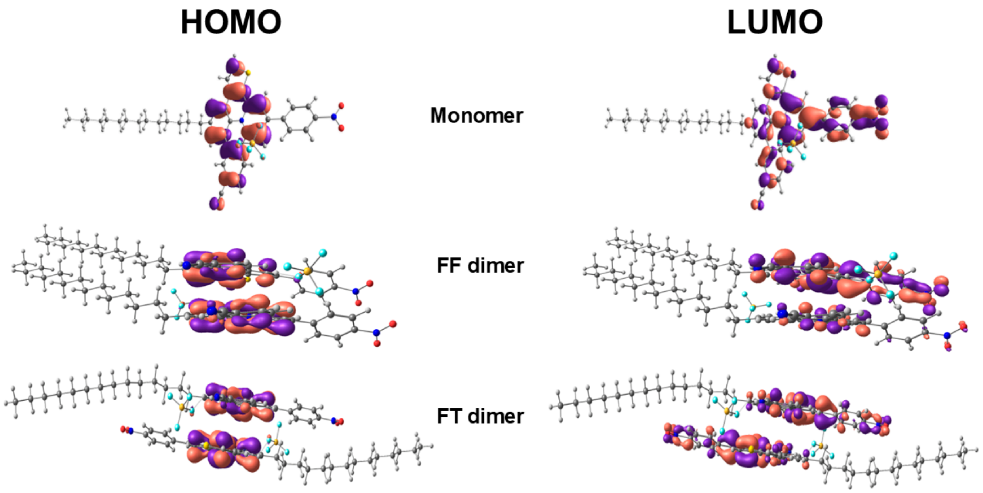


Figure 2. Frontier molecular orbital distributions in the gas phase of compound **4** calculated for the monomeric and π-stacked dimeric models.

Two dimeric arrangements were considered: a face-to-face (FF) model and a face-to-tail (FT) model, selected as representative π-stacked motifs previously considered for related cationic polycyclic heteroaromatic salts. The HOMO and LUMO are mainly localized on the fused benzothienoquinolizinium π-system and the electron-withdrawing aryl substituents, with no significant contribution from the tetradecyl alkyl chain (Figure 2). Thus, both the alkyl chain and BF_4^- counterions behave as electronically passive fragments in the frontier molecular orbital description, while the cationic π-core and the nitro/cyano substituents govern the acceptor character of compound **4**.

As summarized in Table 2, the monomer presents calculated HOMO and LUMO energies of −6.85 eV and −3.36 eV, respectively, with an energy gap of 3.49 eV. Upon dimer formation, the LUMO is further stabilized, particularly in the FF arrangement. The FF dimer shows the lowest LUMO energy (−3.99 eV) and the smallest calculated gap (3.00 eV), whereas the FT dimer gives intermediate values, with a LUMO of −3.86 eV and a gap of 3.23 eV. This behavior indicates that π-stacking modulates the frontier electronic structure of compound **4**. In particular, the stronger LUMO stabilization observed for the FF dimer suggests a greater electron-accepting tendency in this stacked arrangement, while the decrease in the HOMO–LUMO gap reflects enhanced intermolecular electronic communication between the π-conjugated cationic cores.

Although the calculated energy gaps should not be directly compared with the experimental optical band gap, the relative decrease observed for the dimeric models supports the relevance of supramolecular organization in modulating the electronic properties of compound **4**.

Table 2. Frontier molecular orbital energies calculated in the gas phase for compound **4** and its π-stacked dimers.

System	HOMO/eV	LUMO/eV	HOMO–LUMO Gap/eV
Monomer **4**	−6.85	−3.36	3.49
Dimer **4**-FF	−7.00	−3.99	3.00
Dimer **4**-FT	−7.09	−3.86	3.23

3.4.2. TD-DFT Absorption Spectra of the Monomeric and Dimeric Models

The electronic absorption properties of compound **4** were further evaluated by TD-DFT calculations in the gas phase. The simulated spectra were analyzed for the monomeric model and for the two π-stacked dimeric arrangements, namely face-to-face (FF) and face-to-tail (FT). Although the experimental UV–Vis spectrum was recorded in CH_2Cl_2, the gas-phase TD-DFT calculations provide useful qualitative information on the electronic transitions responsible for the absorption profile and the effect of π-stacking on the low-energy region.

For the monomer of **4**, the calculated spectrum reproduces the intense transitions in the UV region, mainly between approximately 320 and 350 nm, in reasonable qualitative agreement with the experimental absorption profile (Figure 3). More importantly, the lowest energy calculated transition with appreciable oscillator strength appears in the visible-near-UV region, around 420 nm. This transition is the most relevant for the electronic excitation analysis because it is the closest one to the experimental low energy absorption tail and to the optical onset observed for compound **4**. Therefore, this transition was selected for a more detailed electron–hole and charge-transfer analysis.

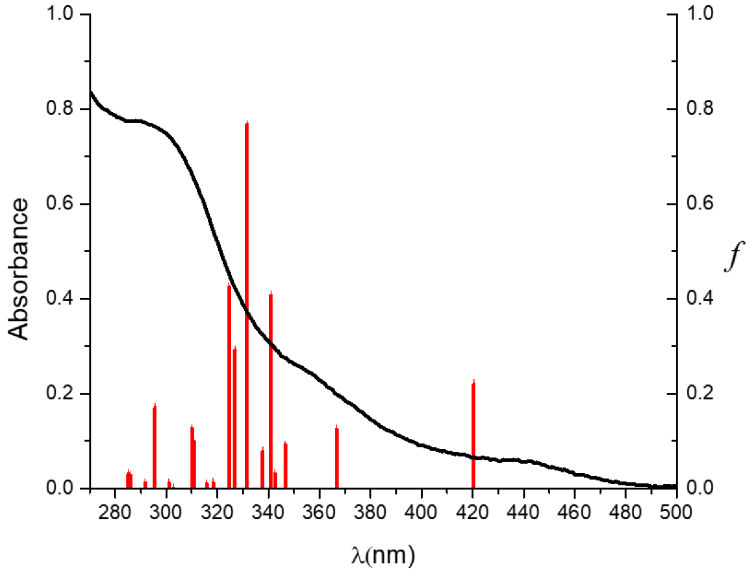


Figure 3. Experimental UV–Vis absorption spectrum of compound **4** in CH_2Cl_2 compared with the calculated TD-DFT vertical transitions of the monomeric model in the gas phase. The theoretical oscillator strengths (*f*) have been normalized to the maximum experimental absorbance to facilitate direct comparison of the transition energies.

The calculated spectrum of the FF dimer shows a noticeable red shift of the low energy transitions compared with the monomer. In particular, transitions appear in the visible region, around 450–470 nm (Figure S13), consistent with the previously observed reduction of the HOMO–LUMO gap for this π-stacked arrangement. This behavior suggests that

face-to-face aggregation can generate lower-energy excited states through intermolecular electronic coupling between the stacked cationic π-cores.

A similar but less pronounced behavior is observed for the FT dimer, which also displays low-energy transitions in the visible region near 450–460 nm (Figure S15). However, the most intense transitions remain located in the UV region. This indicates that both dimeric arrangements can contribute to the red-shifted absorption region, but the FF arrangement appears to promote stronger low-energy electronic communication, in agreement with the frontier orbital analysis.

Overall, the TD-DFT results suggest that the experimental absorption tail of compound **4** may arise not only from the intrinsic low-energy transition of the monomeric benzothienoquinolizinium cation, but also from possible contributions of π-stacked aggregates. This interpretation is consistent with the known tendency of related planar cationic polycyclic aromatic systems to form π-stacked assemblies [32]. Therefore, the monomeric low-energy transition around 418 nm was used as the main transition for the subsequent excitation analysis, while the dimeric calculations support the possible role of aggregation in extending the absorption toward the visible region [31,32]. Based on this analysis, the lowest energy monomeric transition with appreciable oscillator strength was selected for the electron excitation analysis, since it is the transition most directly associated with the low energy absorption response of compound **4**. Additional TD-DFT calculations were performed using CAM-B3LYP-D3/6-311G(d) with the SMD continuum model for acetonitrile to evaluate the sensitivity of the excited-state assignments to long-range exchange and solvent polarization. As expected, the long-range-corrected functional produced a blue shift (Figures S12, S14 and S16) of the selected transitions and larger orbital energy gaps compared with B3LYP (Table S3). Therefore, the CAM-B3LYP results were not used for direct quantitative comparison with the electrochemical energy levels.

3.4.3. Electron Excitation Analysis

To further understand the nature of the low-energy electronic transitions of compound **4**, electron excitation analyses were performed using Multiwfn [45,46,61]. The analysis was focused on the most relevant visible transitions ($f > 0$) obtained from the TD-DFT spectra of the monomer and the two π-stacked dimeric models in the gas phase (Figure 4). In the monomer, the lowest-energy transition appears at approximately 418 nm and was previously identified as the most relevant transition for the optical response of the nitro- and cyano-functionalized benzothienoquinolizinium salt. This transition presents a dominant local excitation character, although with a non-negligible charge-transfer contribution.

For the monomer, the $S_0 \rightarrow S_1$ transition displays 77.6% local excitation (LE) and 22.4% charge-transfer (CT) character in Table 3. Although the excitation is predominantly localized, the calculated Δr value of 2.11 Å indicates a significant spatial displacement between the hole and electron distributions. This value is relevant because Δr values above approximately 2 Å [66] are commonly interpreted as evidence of charge-transfer character. Therefore, the monomeric transition can be described as a mixed LE/CT excitation, mainly localized on the fused benzothienoquinolizinium scaffold but involving electron-density displacement toward the nitro- and cyano-substituted acceptor regions.

The dimeric models show a clear increase in CT character in Table 3. In the face-to-face dimer, the selected $S_0 \rightarrow S_2$ and $S_0 \rightarrow S_3$ transitions display CT contributions of 51.6% and 53.8%, respectively. These values are substantially higher than that observed for the monomer, indicating that π-stacking promotes stronger intermolecular charge redistribution. This is also supported by the Δr values of 3.57 Å and 2.45 Å, which are both above the 2 Å threshold and therefore consistent with charge-transfer transitions. The $S_0 \rightarrow S_2$ transition of the FF dimer is especially relevant because it combines the

largest Δr value with the lowest calculated exciton binding energy, expressed by the electron–hole Coulomb attraction energy ($E_{coulomb}$ = 2.68 eV). This result indicates a more spatially separated electron–hole pair and weaker electron–hole binding compared with the monomer.

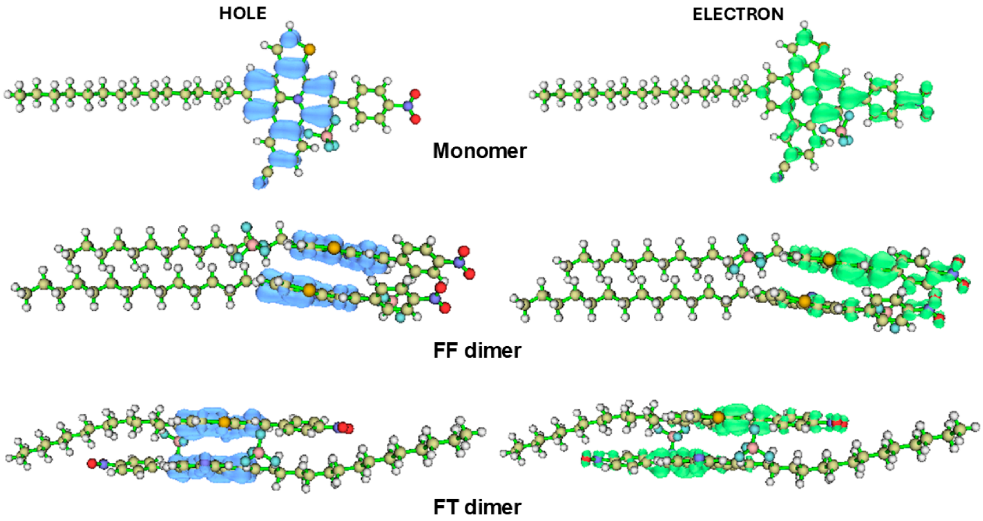


Figure 4. Hole (blue) and electron (green) distribution maps for the selected low-energy transitions of compound **4** and its π-stacked dimeric models calculated in the gas phase.

Table 3. Electron excitation descriptors for the selected low-energy transitions of compound **4** and its π-stacked dimers in the gas phase.

Molecules	Transition	λ/nm	(Δr/Å)	($E_{coulomb}$/eV)	LE/%	CT/%
Monomer 4	$S_0 \rightarrow S_1$	418.3	2.11	3.48	77.6	22.4
Dimer 4-FF	$S_0 \rightarrow S_2$	465.4	3.57	2.69	48.4	51.6
Dimer 4-FF	$S_0 \rightarrow S_3$	453.3	2.45	2.99	46.3	53.7
Dimer 4-FT	$S_0 \rightarrow S_2$	454.1	0.027	2.85	50.0	50.0
Dimer 4-FT	$S_0 \rightarrow S_4$	449.8	0.027	2.83	48.9	51.1

By contrast, the face-to-tail dimer also shows approximately balanced LE/CT percentages, with CT values close to 50%. However, the Δr values are very small, approximately 0.027 Å, indicating that the global centroids of the hole and electron distributions remain nearly coincident. This means that although the electronic redistribution has a CT character according to the fragment-based analysis, the opposite orientations of the two stacked molecules likely produces a partial cancellation of the net charge displacement. Therefore, the FT transitions should not be interpreted as long-range directional CT transitions. Rather, they correspond to more symmetric or compensated electronic redistributions within the dimeric arrangement.

The $E_{coulomb}$ values also support the effect of aggregation on the excited-state character. The monomer shows the highest calculated Coulombic attraction energy (3.48 eV), consistent with a more localized excitation and stronger electron–hole interaction. In contrast, the dimeric models show lower values, ranging from 2.68 to 3.00 eV for the FF dimer and around 2.83–2.85 eV for the FT dimer. The reduction of $E_{coulomb}$ upon dimer formation suggests that π-stacking decreases the electron–hole attraction, most likely due to increased spatial delocalization and intermolecular electronic coupling. This effect is particularly important for organic semiconductor candidates, since lower exciton binding can favor charge separation in donor–acceptor environments.

Overall, **4** exhibits a mixed LE/CT transition in the visible region, while π-stacked dimers, especially the FF arrangement, enhance CT character and reduce the Coulombic attraction between the hole and electron distributions. These results support the relevance of molecular aggregation in modulating the excited-state properties of this benzothienoquinolizinium tetrafluoroborate and reinforce its potential as an electron-accepting π-conjugated material. Additional CAM-B3LYP-D3/6-311G(d)/SMD(CH_3CN) calculations did not significantly alter the hole and electron density distributions (Figure S17). Although the absolute excitation energies are method dependent, the same qualitative trend was preserved: the π-stacked dimers retain enhanced CT character relative to the monomer and exhibit lower electron–hole Coulomb attraction energies (Table S3). These results further support the conclusion that π-stacking can modulate the excited-state character of compound **4**.

3.4.4. Charge-Transport Parameters from Marcus Theory

Charge-transport parameters were estimated for the two π-stacked dimeric models of compound **4** using the Marcus formalism [31,47–56]. All transport descriptors, including electronic couplings, reorganization energies, charge-transfer rate constants, and relative mobilities, were obtained from the M06-2X/6-311G(d) optimized geometries of the face-to-face (FF) and face-to-tail (FT) dimers. This analysis was performed to evaluate how the relative molecular orientation affects the electron- and hole-transport tendencies of the photocyclised benzothienoquinolizinium salt.

The electron-transfer rate constants were estimated according to Equation (5):

$$k_{ET} = \frac{t^2}{\hbar}\left(\frac{\pi}{\lambda k_B T}\right)^{1/2} exp\left(-\frac{\lambda}{4k_B T}\right) \quad (5)$$

where t is the electronic coupling, λ is the reorganization energy, k_B is the Boltzmann constant, T is the temperature, and $\hbar$ is the reduced Planck constant. Relative charge-carrier mobilities were then estimated from the corresponding charge-transfer rates and intermolecular distances.

After the charge-transfer rate constants were obtained, the relative charge-carrier mobilities were estimated using the Einstein relation for a one-dimensional hopping process:

$$\mu = \frac{eD}{k_B T} = \frac{el^2}{k_B T} k_{ET} \quad (6)$$

where (e) is the elementary charge, (D) is the diffusion coefficient, (l) is the intermolecular hopping distance between adjacent monomeric units, and (k_{ET}) is the charge-transfer rate constant obtained from Marcus theory. The calculated mobility values obtained from Equation (6) should therefore be considered comparative descriptors of electron and hole transport tendencies within the FF and FT dimeric arrangements, rather than absolute device mobilities.

The calculated parameters are summarized in Table 4. For the face-to-face (FF) dimer, the electron reorganization energy λ_e is lower than the hole reorganization energy λ_h (0.458 eV vs. 0.586 eV), which favors electron transport from an energetic relaxation perspective. Although the hole electronic coupling t_h is larger than t_e, the resulting electron and hole transfer rates are of the same order of magnitude. Consequently, the calculated mobilities are relatively balanced, with $\mu_e = 9.00 \times 10^{-2}$ cm^2 V^{-1} s^{-1} and $\mu_h = 7.66 \times 10^{-2}$ cm^2 V^{-1} s^{-1}. This indicates an almost ambipolar behavior for the FF arrangement, with a slight preference for electron transport.

Table 4. Charge-transport parameters calculated in the gas phase for the π-stacked dimeric models of compound **4** using Marcus theory. The FF and FT dimer geometries were optimized at the M06-2X/6-311G(d) level. The calculations were performed at T = 298.15 K using the intermolecular hopping distances obtained from the optimized FF (3.30×10^{-8} cm) and FT (3.36×10^{-8} cm) dimer geometries.

Dimer	t_e/Ev	λ_e/eV	k_{ET}^e/s^{-1}	μ_e/cm^2 V^{-1} s^{-1}	t_h/eV	λ_h/eV	k_{ET}^h/s^{-1}	μ_h/cm^2 V^{-1} s^{-1}
Dimer FF	0.086	0.458	2.12×10^{12}	9.00×10^{-2}	0.157	0.586	1.80×10^{12}	7.66×10^{-2}
Dimer FT	0.003	0.590	5.72×10^{8}	2.51×10^{-5}	0.014	0.330	2.17×10^{11}	9.53×10^{-3}

In contrast, the face-to-tail (FT) dimer shows a markedly different behavior in Table 4. The electron coupling t_e decreases drastically to 0.003 eV, while the electron reorganization energy increases to 0.590 eV. As a result, the calculated electron-transfer rate and mobility decrease significantly, giving $\mu_e = 2.51 \times 10^{-5}$ cm^2 V^{-1} s^{-1}. For holes, the lower reorganization energy $\lambda_h = 0.330$ eV and larger coupling $t_h = 0.014$ eV lead to a much higher hole mobility of $\mu_h = 9.53 \times 10^{-3}$ cm^2 V^{-1} s^{-1}. Thus, the FT arrangement is predicted to favor hole transport rather than electron transport.

These results show that the charge-transport behavior of compound **4** is highly sensitive to the supramolecular arrangement. The FF packing model is the most favorable for electron transport and gives nearly balanced electron/hole mobilities, whereas the FT model leads to a predominantly hole-transporting pathway. Therefore, the potential N-type character of compound **4** should be mainly associated with its low-lying electrochemical LUMO and electron-deficient nitro/cyano-functionalized cationic framework, while its actual charge-transport polarity is expected to depend strongly on the solid-state packing motif. This reinforces the importance of future thin-film or crystallographic studies to determine the preferred packing arrangement and validate its semiconductor behavior experimentally.

Theoretical calculations suggest that while the molecule is designed as an acceptor, its charge-transport character may be highly packing-dependent.

3.4.5. Donor–Acceptor Interaction with Hexaphenyl-Substituted Hexabenzocoronene

To explore the potential compatibility of compound **4** with discotic donor materials, a preliminary donor–acceptor model was constructed using hexaphenyl-substituted hexabenzocoronene (HBC-PhC$_{12}$) as a representative π-discotic donor. This model was inspired by previous reports on HBC-PhC$_{12}$/perylene photovoltaic systems, in which self-organized discotic donor–acceptor blends exhibited efficient photoinduced charge transfer and transport via segregated π-stacked domains [67–69]. In these systems, HBC derivatives act mainly as hole-transporting discotic donors, while electron-deficient aromatic compounds serve as acceptor components [44,46,53,55].

The isolated HBC-PhC$_{12}$ donor, compound **4**, and the HBC-PhC$_{12}$···**4** donor–acceptor complex were optimized at the M06-2X/6-31G(d,p) level. Single-point calculations were then performed at the B3LYP/6-311G(d) level on the optimized geometries to analyze the frontier molecular orbitals and donor–acceptor alignment. The calculated orbital distribution of the HBC-PhC$_{12}$···**4** complex shows that the HOMO is mainly localized on the HBC-PhC$_{12}$ donor at the bottom, whereas the LUMO is localized on the nitro- and cyano-functionalized, tetradecyl-substituted benzothienoquinolizinium tetrafluoroborate acceptor **4** at the top (Figure 5). This HOMO-on-donor/LUMO-on-acceptor distribution is consistent with a type-II-like donor–acceptor orbital alignment and suggests that photoinduced charge transfer from HBC to compound **4** may be energetically feasible.

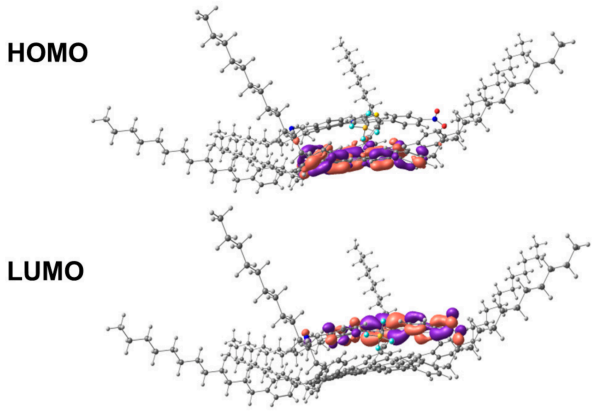


Figure 5. Frontier molecular orbital distributions of the HBC-PhC$_{12}$···**4** donor–acceptor complex obtained from single point B3LYP/6-311G(d) calculations on the M06-2X/6-31G(d,p)-optimized geometry in the gas phase.

The calculated gas-phase HOMO level of HBC-PhC$_{12}$ was −5.29 eV, in close agreement with the literature HOMO value of −5.25 eV reported for HBC-PhC$_{12}$ from thin film cyclic voltammetry [67]. This agreement supports the use of the calculated donor level as a qualitative reference for the HBC-PhC$_{12}$···**4** donor–acceptor model. For compound **4**, the calculated gas-phase LUMO was −3.36 eV, whereas the electrochemically estimated LUMO level in acetonitrile was −3.87 eV. Although these values (Table 5) should not be considered directly equivalent, together they support the electron-deficient character of compound **4** and its qualitative energetic compatibility with HBC-PhC$_{12}$-type donors.

Table 5. Frontier energy levels used to evaluate the qualitative donor–acceptor alignment between HBC-PhC$_{12}$ and compound **4**.

Energy Level	Value/eV	Source/Approach
HOMO of HBC-PhC$_{12}$	−5.29	B3LYP/6-311G(d), gas phase, this work
HOMO of HBC-PhC$_{12}$	−5.25	Literature, thin-film CV [67]
LUMO of compound **4**	−3.36	B3LYP/6-311G(d), gas phase, this work
LUMO of compound **4**	−3.87	Experimental CV in CH_3CN, this work

Note: The energy levels are used only as approximate descriptors of donor–acceptor energetic compatibility. Gas phase Kohn–Sham orbital energies and electrochemically derived frontier levels are not directly equivalent quantities. The literature HOMO level of HBC-PhC$_{12}$ was obtained from thin film cyclic voltammetry, whereas the LUMO level of compound **4** was estimated from cyclic voltammetry in acetonitrile. Therefore, these values should not be interpreted as directly comparable device parameters or as predicted photovoltaic performance.

The electron excitation analysis of the HBC-PhC$_{12}$···**4** complex was performed for the HOMO→LUMO transition [45,46,56,61]. In Table 6, this transition appears at 1.67 eV, corresponding to approximately 744 nm, and displays a strong intermolecular charge-transfer character. The electron–hole separation descriptor Δr is 3.96 Å, indicating a clear spatial displacement between the hole and electron distributions. The hole is mainly localized on the HBC-PhC$_{12}$ donor at the bottom, whereas the electron is transferred toward the benzothienoquinolizinium acceptor 4 at the top (Figure 6). This interpretation is consistent with the fragment analysis, which gives a dominant CT contribution of approximately 97.8% and only 2.2% local excitation character.

The electron–hole Coulomb attraction energy is 2.26 eV, lower than that obtained for the isolated monomeric acceptor transition discussed above. This decrease is consistent with a more spatially separated electron–hole pair in the HBC-PhC$_{12}$···**4** complex. In other words,

the donor–acceptor interaction not only produces a HOMO-on-HBC-PhC$_{12}$/LUMO-on-acceptor orbital distribution, but also generates an excited state with strong intermolecular CT character, significant electron–hole separation, and reduced Coulombic attraction. These features support the potential role of compound **4** as an electron-accepting partner in discotic donor–acceptor assemblies.

Table 6. Electron excitation descriptors for the selected $S_0 \rightarrow S_1$ transition of the HBC-PhC$_{12}$···**4** donor–acceptor complex in the gas phase.

Model	Transition	λ/nm	(Δr/Å)	($E_{coulomb}$/eV)	LE/%	CT/%
HBC-PhC$_{12}$···**4**	$S_0 \rightarrow S_1$	744.06	3.96	2.26	2.20	97.8

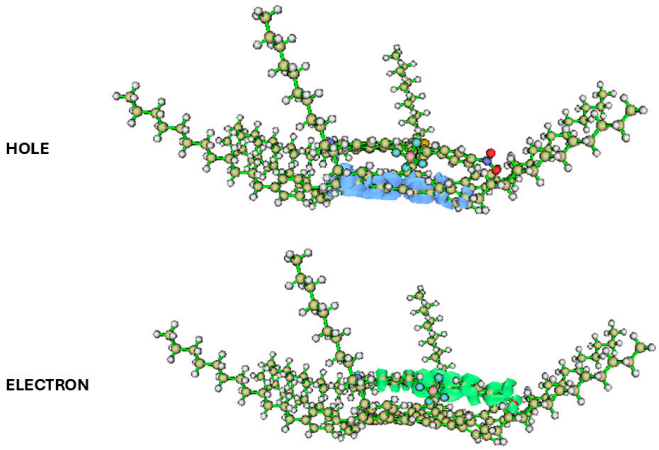


Figure 6. Hole and electron distribution maps for the selected HOMO→LUMO transition of the HBC-PhC$_{12}$···**4** complex calculated in the gas phase. The hole distribution map is shown in blue and the electron distribution map in green.

To evaluate the robustness of this charge-transfer assignment, an additional TD-DFT calculation was performed for the HBC-PhC$_{12}$···**4** complex at the CAM-B3LYP-D3/6-311G(d) level using the SMD continuum model for acetonitrile. As expected for a long-range-corrected functional, the selected transition was blue shifted relative to the B3LYP result (Table S4). However, the qualitative excited-state description was preserved: the transition retained a dominant intermolecular CT character, with a CT contribution of 96.8%, a low LE contribution of 3.2%, and a reduced electron–hole Coulomb attraction energy of 2.21 eV. The corresponding data are provided in Table S4. These results reinforce the robustness of the qualitative donor–acceptor CT assignment for the HBC-PhC$_{12}$···**4** complex. The CAM-B3LYP-D3/6-311G(d)/SMD(CH_3CN) calculation also preserved the qualitative donor–acceptor electronic picture of the HBC-PhC$_{12}$···**4** complex. The frontier orbital distributions remained similar, with the HOMO mainly localized on HBC-PhC$_{12}$ and the LUMO on compound 4 (Figure S18). The corresponding hole/electron distribution maps also retained the same spatial separation, with hole on the donor and electron on the acceptor (Figure S19). This supports the soundness of the intermolecular CT assignment under solvent polarized conditions.

4. Conclusions

In this work, a nitro- and cyano-functionalized benzothienoquinolizinium tetrafluoroborate was synthesized by oxidative photocyclisation of a pyridinium precursor and evaluated as a potential small molecule organic semiconductor. To ensure consistency with the electrochemical analysis, the UV–Vis spectra were recorded in acetonitrile, the same

solvent used for cyclic voltammetry. Photocyclisation produced a marked red shift in the absorption profile and reduced the optical band gap from 3.19 eV for precursor **3** to 2.61 eV for the fused benzothienoquinolizinium salt **4**. Cyclic voltammetry revealed a stabilized electrochemical LUMO level of approximately −3.87 eV for compound **4**, supporting the electron deficient character of the photocyclised scaffold.

Theoretical calculations showed that the frontier molecular orbitals are localized mainly on the fused cationic π-system and the nitro/cyano substituted aryl fragments, with negligible contribution from the tetradecyl chain and BF_4^- counterion. TD-DFT and electron excitation analyses indicated that the low-energy transition of monomeric salt **4** has mixed local/charge-transfer character, whereas the π-stacked dimers, particularly the face to face arrangement, exhibit enhanced CT character and reduced electron–hole Coulombic attraction. Additional CAM-B3LYP-D3/SMD(CH_3CN) calculations, included in the Supporting Information, confirmed that these qualitative trends are preserved upon inclusion of long-range exchange and solvent polarization, although the absolute transition energies are method dependent. Marcus type charge transport calculations further showed that the FF dimer exhibits nearly ambipolar transport with a slight electron preference, while the FT dimer favors hole transport.

In addition, a donor–acceptor model with HBC-PhC_{12} was evaluated to explore the compatibility of compound **4** with discotic donor materials. The HBC-PhC_{12}···**4** complex showed a HOMO localized mainly on the HBC-PhC_{12} donor and a LUMO localized mainly on the benzothienoquinolizinium acceptor, consistent with a donor–acceptor orbital arrangement favorable for intermolecular charge transfer. The donor–acceptor comparison was discussed in terms of qualitative frontier energy level alignment, using the calculated and literature HOMO levels of HBC-PhC_{12} together with the calculated and electrochemically estimated LUMO levels of compound **4**. This analysis supports the qualitative energetic compatibility between HBC-PhC_{12} and compound **4**, without implying direct prediction of photovoltaic device performance. Electron excitation analysis of the HBC-PhC_{12}···**4** complex also revealed strong intermolecular CT character, significant electron–hole separation, and reduced Coulombic attraction; this assignment was further supported by CAM-B3LYP-D3/SMD(CH_3CN) calculations provided in the Supporting Information.

Overall, these results indicate that compound **4** is an electron-deficient cationic π-conjugated scaffold with promising features for N-type organic semiconductor design. Its low lying electrochemical LUMO, visible region absorption, CT active excited states, and qualitative energetic compatibility with HBC-PhC_{12} support its potential as an acceptor component in future organic optoelectronic materials. However, the effective charge-transport polarity and photovoltaic relevance of this system are expected to depend strongly on molecular packing, thin film organization, and donor–acceptor morphology. Future studies should therefore focus on evaluating the solid-state organization, thin film morphology, and donor–acceptor assembly behavior of compound **4** in order to clarify how supramolecular arrangement affects charge transport and optoelectronic response.

Supplementary Materials: The following supporting information can be downloaded at https://www.mdpi.com/article/10.3390/cryst16090575/s1, Figure S1: ^{1}H NMR spectrum of pyridinium salt precursor **3**; Figure S2: ^{13}C NMR spectrum of pyridinium salt precursor **3**; Figure S3: DSC thermogram of compound **3**; Figure S4: ^{1}H NMR spectrum of photocyclised benzothienoquinolizinium tetrafluoroborate **4**; Figure S5: ^{13}C NMR spectrum of photocyclised benzothienoquinolizinium tetrafluoroborate **4**; Figure S6: DSC thermogram of compound **4**; Figure S7: cyclic voltammogram of the blank supporting-electrolyte solution; Figure S8: cyclic voltammogram of the Fc/Fc^+ redox couple; Figure S9: cyclic voltammogram of pyridinium salt precursor **3**; Figure S10: cyclic voltammogram of compound **4**; Table S1: BSSE-corrected interaction energies for representative FF and FT π-stacked arrangements of the parent BTQ scaffold; Figure S11: selected FF and FT π-stacked

arrangements from the BF_4^- counterion conformational screening; Table S2: frontier molecular orbital energies calculated at the CAM-B3LYP-D3/6-311G(d)/SMD(CH_3CN) level; Figures S12–S16: simulated TD-DFT absorption spectra of compound **4** and its FF and FT π-stacked dimers (gas phase and SMD(CH_3CN)); Table S3: electron excitation descriptors for compound **4** and its π-stacked dimers calculated at the CAM-B3LYP-D3/6-311G(d)/SMD(CH3CN) level; Figure S17: hole and electron distribution maps for compound **4** and its π-stacked dimeric models calculated at the CAM-B3LYP-D3/6-311G(d)/SMD(CH_3CN) level; Figure S18: frontier molecular orbital distributions of the HBC-PhC_{12}···**4** donor–acceptor complex; Table S4: electron excitation descriptors for the HBC-PhC_{12}···**4** donor–acceptor complex calculated at the CAM-B3LYP-D3/6-311G(d)/SMD(CH_3CN) level; Figure S19: hole and electron distribution maps for the HBC-PhC_{12}···**4** donor–acceptor complex.

Author Contributions: Conceptualization, A.A. and K.W.-A.; methodology, A.A., K.P. and K.W.-A.; software, A.A. and K.W.-A.; validation, A.A., F.A.A. and K.W.-A.; formal analysis, A.A. and K.W.-A.; investigation, A.A., K.P., D.V., I.C., J.G., C.Z. and S.E.; resources, A.A. and F.A.A.; data curation, A.A., K.P., D.V., I.C., J.G., C.Z. and S.E.; writing—original draft preparation. A.A.; writing—review and editing, A.A., K.W.-A. and F.A.A.; visualization, A.A., K.W.-A. and D.V.; supervision, A.A., K.P. and F.A.A.; project administration, A.A.; funding acquisition, A.A. All authors have read and agreed to the published version of the manuscript.

Funding: This research was funded by ANID, Chile, FONDECYT de Iniciacion 11220544. The APC was funded by Vicerrectoría de Investigación de Universidad de Las Américas.

Data Availability Statement: The original contributions presented in this study are included in the article/Supplementary Material. Further inquiries can be directed to the corresponding author.

Acknowledgments: This research was supported by the Fondo Nacional de Desarrollo Científico y Tecnológico (FONDECYT), project number 11220544 (A.A.). K.W.-A. acknowledges support from FONDECYT project number 11250831. S.E. acknowledges support from FONDECYT project number 1230872. This research was partially supported by the supercomputing infrastructure of the NLHPC (ECM-02). The support of the high-performance computing system of PIDi-UTEM (SCC-PIDi-UTEM CONICYT-FONDEQUIP EQM180180) is gratefully acknowledged. During the preparation of this manuscript, the authors used OpenAI ChatGPT (GPT-5.5 Thinking) for language polishing, grammar correction, and editorial refinement. The tool was not used to generate experimental data, perform calculations, interpret results, or draw scientific conclusions.

Conflicts of Interest: The authors declare no conflicts of interest.

References

1. Köhler, A.; Bässler, H. *Electronic Processes in Organic Semiconductors*; Wiley-VCH: Weinheim, Germany, 2015. [CrossRef]
2. Alcácer, L. Organic semiconductors for organic electronics. In *The Physics of Organic Electronics*; Chapter 7; IOP Publishing: Bristol, UK, 2022. [CrossRef]
3. Köhler, A.; Bässler, H. The electronic structure of organic semiconductors. In *Electronic Processes in Organic Semiconductors: An Introduction*; Wiley-VCH: Weinheim, Germany, 2015; pp. 1–86. [CrossRef]
4. Bi, P.; Ren, J.; Zhang, S.; Wang, J.; Hou, J. PTV-based p-type organic semiconductors: Candidates for low-cost photovoltaic donors with simple synthetic routes. *Polymer* **2020**, *209*, 122900. [CrossRef]
5. Okamoto, T.; Yu, C.P.; Mitsui, C.; Yamagishi, M.; Ishii, H.; Takeya, J. Bent-shaped p-type small-molecule organic semiconductors: A molecular design strategy for next-generation practical applications. *J. Am. Chem. Soc.* **2020**, *142*, 9083–9096. [CrossRef] [PubMed]
6. Mumyatov, A.V.; Troshin, P.A. A review on fullerene derivatives with reduced electron affinity as acceptor materials for organic solar cells. *Energies* **2023**, *16*, 1924. [CrossRef]
7. Chen, J.; Chen, Y.; Feng, L.-W.; Gu, C.; Li, G.; Su, N.; Wang, G.; Swick, S.M.; Huang, W.; Guo, X.; et al. Hole (donor) and electron (acceptor) transporting organic semiconductors for bulk-heterojunction solar cells. *EnergyChem* **2020**, *2*, 100042. [CrossRef]
8. Li, X.; Kong, X.; Sun, G.; Li, Y. Organic small-molecule acceptor materials for organic solar cells. *eScience* **2023**, *3*, 100171. [CrossRef]
9. Speller, E.M.; Clarke, A.J.; Luke, J.; Lee, H.K.H.; Durrant, J.R.; Li, N.; Wang, T.; Wong, H.C.; Kim, J.-S.; Tsoi, W.C.; et al. From fullerene acceptors to non-fullerene acceptors: Prospects and challenges in the stability of organic solar cells. *J. Mater. Chem. A.* **2019**, *7*, 23361–23377. [CrossRef]

10. Ike, J.N.; Mola, G.T.; Taziwa, R.T. Review on indacenodithiophene (IDT)- and perylene diimide (PDI)-based non-fullerene acceptors in organic solar cells: Progress and challenges. *Chem. Afr.* **2025**, *8*, 2687–2705. [CrossRef]
11. Li, Q.; Zhang, Y.; Xie, Z.; Zhen, Y.; Hu, W.; Dong, H. Polycyclic aromatic hydrocarbon-based organic semiconductors: Ring-closing synthesis and optoelectronic properties. *J. Mater. Chem. C* **2022**, *10*, 2411–2430. [CrossRef]
12. Stępień, M.; Gońka, E.; Żyła, M.; Sprutta, N. Heterocyclic nanographenes and other polycyclic heteroaromatic compounds: Synthetic routes, properties, and applications. *Chem. Rev.* **2017**, *117*, 3479–3716. [CrossRef] [PubMed]
13. Kilaru, S.; Gade, R.; Bhongiri, Y.; Tripathi, A.; Chetti, P.; Pola, S. Organic materials based on hetero-polycyclic aromatic hydrocarbons for organic thin-film transistor applications. *Mater. Sci. Semicond. Process.* **2022**, *147*, 106730. [CrossRef]
14. Feng, X.; Marcon, V.; Pisula, W.; Hansen, M.R.; Kirkpatrick, J.; Grozema, F.; Andrienko, D.; Kremer, K.; Müllen, K. Towards high charge-carrier mobilities by rational design of the shape and periphery of discotics. *Nat. Mater.* **2009**, *8*, 421–426. [CrossRef] [PubMed]
15. Pisula, W.; Feng, X.; Müllen, K. Tuning the columnar organization of discotic polycyclic aromatic hydrocarbons. *Adv. Mater.* **2010**, *22*, 3634–3649. [CrossRef] [PubMed]
16. Kumar, M.; Kumar, S. Liquid crystals in photovoltaics: A new generation of organic photovoltaics. *Polym. J.* **2017**, *49*, 85–111. [CrossRef]
17. Xie, L.; Jiang, Y.; Chen, L.; Qiu, D.; Yi, J.; Yu, H.; Zhang, J.; Wei, Z.; Lai, J.Y.L.; Liu, S.; et al. Incorporation of an extended electron-deficient central block into small-molecule acceptors toward enhanced-performance organic solar cells. *Aggregate* **2026**, *7*, e70355. [CrossRef]
18. Wu, D.; Liu, R.; Pisula, W.; Feng, X.; Müllen, K. Two-Dimensional Nanostructures from Positively Charged Polycyclic Aromatic Hydrocarbons. *Angew. Chem. Int. Ed.* **2011**, *50*, 2791–2794. [CrossRef] [PubMed]
19. Wu, D.; Pisula, W.; Enkelmann, V.; Feng, X.; Müllen, K. Controllable columnar organization of positively charged polycyclic aromatic hydrocarbons by choice of counterions. *J. Am. Chem. Soc.* **2009**, *131*, 9620–9621. [CrossRef] [PubMed]
20. Yang, C.; Wu, D.; Zhao, W.; Ye, W.; Xu, Z.; Zhang, F.; Feng, X. Anion-induced self-assembly of positively charged polycyclic aromatic hydrocarbons towards nanostructures with controllable two-dimensional morphologies. *CrystEngComm* **2016**, *18*, 877–880. [CrossRef]
21. Mali, K.S.; Wu, D.; Feng, X.; Müllen, K.; Van der Auweraer, M.; De Feyter, S. Scanning tunneling microscopy-induced reversible phase transformation in the two-dimensional crystal of a positively charged discotic polycyclic aromatic hydrocarbon. *J. Am. Chem. Soc.* **2011**, *133*, 5686–5688. [CrossRef] [PubMed]
22. Fortage, J.; Tuyèras, F.; Ochsenbein, P.; Puntoriero, F.; Nastasi, F.; Campagna, S.; Griveau, S.; Bedioui, F.; Ciofini, I.; Lainé, P.P. Expanded pyridiniums: Bis-cyclization of branched pyridiniums into their fused polycyclic and positively charged derivatives—Assessing the impact of pericondensation on structural, electrochemical, electronic, and photophysical features. *Chem. Eur. J.* **2010**, *16*, 11047–11063. [CrossRef] [PubMed]
23. Wu, D.; Feng, X.; Takase, M.; Haberecht, M.C.; Müllen, K. Synthesis and self-assembly of dibenzo [*jk*,*mn*] naphtho [2,1,8-*fgh*] thebenidinium derivates. *Tetrahedron* **2008**, *64*, 11379–11386. [CrossRef]
24. Asanuma, Y.; Eguchi, H.; Nishiyama, H.; Tomita, I.; Inagi, S. Synthesis of ring-fused pyridinium salts by intramolecular nucleophilic aromatic substitution reaction and their optoelectronic properties. *Org. Lett.* **2017**, *19*, 1824–1827. [CrossRef] [PubMed]
25. Ma, T.; Yang, Y.; Wang, J.; Cheng, X. Mesomorphism, high-contrast negative fluorosolvatochromism and photoinduced fluorescence conversion of thienylcyanostyrene-pyridinium salts. *Dye. Pigment.* **2024**, *229*, 112281. [CrossRef]
26. Sánchez-Pavón, E.; Recio, J.; Ramirez, M.A.; Batanero, B.; Clays, K.; Mendicuti, F.; Marcelo, G.; Carmona, T.; Castaño, O.; Angelova, S.; et al. Highly efficient unbridged D–A+(D) chromophores based on the quinolizinium cation for nonlinear optical (NLO) applications. *Dyes. Pigment.* **2022**, *205*, 110323. [CrossRef]
27. Chen, J.-B.; Di, Y.-M.; Ye, Y.-J.; Song, Y.-P.; Zhou, J.-H.; You, M.-H.; Zhang, S.-Q.; Lin, M.-J. Conjugated naphthalenediimide-pyridinium salts in donor–acceptor hybrid materials for enhanced photochromic properties. *Inorg. Chem.* **2025**, *64*, 606–616. [CrossRef] [PubMed]
28. Huang, L.; Wang, Q.; Fu, P.; Sun, Y.; Xu, J.; Browne, D.L.; Huang, J. Extended quinolizinium-fused corannulene derivatives: Synthesis and properties. *JACS Au* **2024**, *4*, 1623–1631. [CrossRef] [PubMed]
29. Katritzky, A.R.; Zakaria, Z.; Lunt, E. The photocyclisation of 1,2-diarylpyridinium cations and the photobiscyclisation of 1,2,6-triarylpyridinium cations. *J. Chem. Soc. Perkin Trans. 1.* **1980**, *9*, 1879–1887. [CrossRef]
30. Katritzky, A.R.; Agha, B.; de Ville, G.Z.; Lunt, E.; Knyazhanskii, M.I.; Tymyanskii, Y.R.; Pyshchev, A.I. Photocyclization of 1,2-diaryl- and photobicyclization of 1,2,6-triarylpyridinium cations. *Chem. Heterocycl. Compd.* **1984**, *20*, 1245–1254. [CrossRef]
31. Aracena, A.; Rezende, M.C.; García, M.; Muñoz-Becerra, K.; Wrighton-Araneda, K.; Valdebenito, C.; Celis, F.; Vásquez, O. Alkylated benzodithienoquinolizinium salts as possible non-fullerene organic n-type semiconductors: An experimental and theoretical study. *Materials* **2021**, *14*, 6239. [CrossRef] [PubMed]

32. Aracena, A.; Rezende, M.C.; Encinas, M.V.; Vergara, C.; Vásquez, S.O. Aggregation phenomena in photobicyclised pyridinium salts. *New J. Chem.* **2017**, *41*, 14589–14594. [CrossRef]
33. Azizi, A.; Ebrahimi, A. Theoretical investigation of the π+–π+ stacking interactions in substituted pyridinium ion. *J. Mol. Graph. Model.* **2017**, *77*, 225–231. [CrossRef] [PubMed]
34. Cho, Y.; Sun, Z.; Li, G.; Zhang, D.; Yang, S.; Marks, T.J.; Yang, C.; Facchetti, A. CF_3-functionalized side chains in nonfullerene acceptors promote electrostatic interactions for highly efficient organic solar cells. *J. Am. Chem. Soc.* **2024**, *147*, 758–769. [CrossRef] [PubMed]
35. Zahra, S.; Ryu, D.H.; Ha, J.-W.; Lee, S.; Haris, M.; Song, C.E.; Lee, H.K.; Lee, S.K.; Shin, W.S. Trifluorophenyl side-chain engineering in benzotriazole-core acceptors for high-performance organic photovoltaics. *Energy Environ. Mater.* **2025**, *8*, e12875. [CrossRef]
36. Cheng, Y.; Xu, J.; Liang, S.; Li, M.; Wang, B.; Fang, H.; Tan, Q.; Wang, H.; Lu, Z.; Xiao, C.; et al. Asymmetrically trifluoromethylated non-fused electron acceptor for high-efficiency and stable organic solar cells. *ACS Appl. Mater. Interfaces* **2025**, *17*, 45990–45998. [CrossRef] [PubMed]
37. Bauch, F.; Ni, X.; Pratik, S.M.; Nanayakkara, S.; Wang, T.; Brédas, J.-L.; Schumacher, S.; Coropceanu, V. Electronic properties of organic solar cells based on CF_3-functionalized non-fullerene acceptors. *ACS Appl. Mater. Interfaces* **2026**, *18*, 2200–2211. [CrossRef] [PubMed]
38. Wang, J.; Ding, Y.; Li, C.; Zheng, N.; Xie, Z.; Ma, Z.; Lu, Y.; Wan, X.; Chen, Y. Effect of nitro-substituted ending groups on the photovoltaic properties of nonfullerene acceptors. *ACS Appl. Mater. Interfaces* **2020**, *12*, 41861–41868. [CrossRef] [PubMed]
39. Che, Y.; Niazi, M.R.; Yu, T.; Maris, T.; Liu, C.-H.; Ma, D.; Izquierdo, R.; Perepichka, I.F.; Perepichka, D.F. Nitrofluorene-based A–D–A electron acceptors for organic photovoltaics. *J. Mater. Chem. C* **2023**, *11*, 8186–8195. [CrossRef]
40. Wang, H.; Zhao, C.; Burešová, Z.; Bureš, F.; Liu, J. Cyano-capped molecules: Versatile organic materials. *J. Mater. Chem. A* **2023**, *11*, 3753–3770. [CrossRef]
41. Amna, B.; Isci, R.; Faraji, S.; Majewski, L.A.; Ozturk, T. Effects of electron-withdrawing substituents ($-NO_2$, $-F$, and $-CN$) on thieno [3,2-b]thiophene and benzothiadiazole polymers for low-voltage organic transistor and sensor applications. *ACS Appl. Electron. Mater.* **2026**, *8*, 5014–5502. [CrossRef]
42. Zou, X.; Wen, G.; Hu, R.; Dong, G.; Zhang, C.; Zhang, W.; Huang, H.; Dang, W. An insight into the excitation states of small molecular semiconductor Y6. *Molecules* **2020**, *25*, 4118. [CrossRef] [PubMed]
43. Taouali, W.; Alimi, K.; Nangraj, A.S.; Casida, M.E. Density-functional theory (DFT) and time-dependent DFT study of the chemical and physical origins of key photoproperties of end-group derivatives of a nonfullerene acceptor molecule for bulk heterojunction organic solar cells. *J. Comput. Chem.* **2023**, *44*, 2130–2148. [CrossRef] [PubMed]
44. Khan, M.; Sarwar, F.; Gull, K.; Arshad, M.; Shafiq, I.; Arshad, M.N.; Alzahrani, K.A.; Jawaria, R. DFT insights into the photovoltaic performance of A–π–A non-fullerene acceptors for organic solar cells. *Sci. Rep.* **2026**, *16*, 9842. [CrossRef] [PubMed]
45. Yin, G.; Cai, S.; Wang, Y.; Zhao, Z. Theoretical insights into the effect of conjugated cores on optical and photovoltaic properties of small-molecule acceptors for organic solar cells. *ChemistrySelect* **2023**, *8*, e202302652. [CrossRef]
46. Ahmed, R.M.; Adnan, M.; Irshad, Z.; Hussain, R.; Darwish, H.W.; Lim, J. Molecular designing and simulation-driven exploration of benzotrithiophene-based semiconductors for organic photovoltaics. *ChemistrySelect* **2025**, *10*, e202402291. [CrossRef]
47. Bora, S.R.; Kalita, D.J. Molecular engineering of the core part of D–π–A–π–D-based small acceptor molecules for efficient organic solar cells: A DFT approach. *New J. Chem.* **2024**, *48*, 10897–10909. [CrossRef]
48. García, G.; Moral, M.; Granadino-Roldán, J.M.; Garzón, A.; Navarro, A.; Fernández-Gómez, M. Theoretical approach to the study of thiophene-based discotic systems as organic semiconductors. *J. Phys. Chem. C* **2013**, *117*, 15–22. [CrossRef]
49. Rehman, F.U.; Hameed, S.; Khera, R.A.; Shaban, M.; Essid, M.; Aloui, Z.; Al-Saeedi, S.I.; Ibrahim, M.A.A.; Waqas, M. High-efficiency and low-energy-loss organic solar cells enabled by tuning the end-group modification of terthiophene-based acceptor molecules to enhance photovoltaic properties. *ACS Omega* **2023**, *8*, 42492–42510. [CrossRef] [PubMed]
50. Neenu Krishna, P.U.; Muraleedharan, K. Benzothiadiazole-based donor–acceptor–donor-type organic n-type semiconductors: A theoretical study. *Mater. Sci. Semicond. Process.* **2025**, *185*, 108909. [CrossRef]
51. Salwa; Adnan, M.; Irshad, Z.; Hussain, R.; Darwish, H.W.; Hussain, F.; Ahmed, M. Improving optoelectronic properties of acceptor–donor–acceptor-type non-fullerene acceptors containing extended fused-ring donor units for efficient organic semiconductors. *Energy Technol.* **2025**, *13*, e202401529. [CrossRef]
52. Naqvi, S.M.K.A.; Abbas, F.; Bibi, S.; Shehzad, M.K.; Alhokbany, N.; Zhu, Y.; Long, H.; Vasiliev, R.B.; Nazir, Z.; Chang, S. Theoretical investigation of benzodithiophene-based donor molecules in organic solar cells: From structural optimization to performance metrics. *RSC Adv.* **2024**, *14*, 29942–29954. [CrossRef] [PubMed]
53. Mubarik, A.; Shafiq, F.; Ju, X.-H. DFT and TD-DFT study of benzodithiophene-based donor materials with enhanced optoelectronic attributes for organic solar cells. *ChemistrySelect* **2025**, *10*, e202401831. [CrossRef]
54. Rosa, N.; Borges, I., Jr. Review on the DFT computation of bulk heterojunction and dye-sensitized organic solar-cell properties. *J. Mol. Model.* **2025**, *31*, 83. [CrossRef] [PubMed]

55. Zulfiqar, A.; Akhter, M.S.; Waqas, M.; Bhatti, I.A.; Imran, M.; Shawky, A.M.; Shaban, M.; Alotaibi, H.F.; Mahal, A.; Ashour, A.; et al. Engineering of the central core on DBD-based materials with improved power-conversion efficiency using the DFT approach. *ACS Omega* **2024**, *9*, 29205–29225. [CrossRef] [PubMed]
56. Liu, Q.; Xiang, C.; Wu, Q.; Zhou, Z.; Zou, Y.; Liu, W. Theoretical exploration of the molecular stacking and charge-transfer mechanism of PBQx:Y6 organic solar cells. *Surf. Interfaces* **2024**, *44*, 103767. [CrossRef]
57. Rammohan, A.; Reddy, J.S.; Sravya, G.; Rao, C.N.; Zyryanov, G.V. Chalcone synthesis, properties and medicinal applications: A review. *Environ. Chem. Lett.* **2020**, *18*, 433–458. [CrossRef]
58. Mulugeta, D. A review of synthesis methods of chalcones, flavonoids, and coumarins. *Sci. J. Chem.* **2022**, *10*, 41. [CrossRef]
59. Müller, C.; Wasserberg, D.; Weemers, J.J.M.; Pidko, E.A.; Hoffmann, S.; Lutz, M.; Spek, A.L.; Meskers, S.C.J.; Janssen, R.A.J.; van Santen, R.A.; et al. Donor-functionalized polydentate pyrylium salts and phosphinines: Synthesis, structural characterization, and photophysical properties. *Chem. Eur. J.* **2007**, *13*, 4548–4559. [CrossRef] [PubMed]
60. Frisch, M.J.; Trucks, G.W.; Schlegel, H.B.; Scuseria, G.E.; Robb, M.A.; Cheeseman, J.R.; Scalmani, G.; Barone, V.; Petersson, G.A.; Nakatsuji, H.; et al. *Gaussian 16*; Revision B.01; Gaussian, Inc.: Wallingford, CT, USA, 2016.
61. Lu, T.; Chen, F. Multiwfn: A multifunctional wavefunction analyzer. *J. Comput. Chem.* **2012**, *33*, 580–592. [CrossRef] [PubMed]
62. Costa, J.C.S.; Taveira, R.J.S.; Lima, C.F.R.A.C.; Mendes, A.; Santos, L.M.N.B.F. Optical band gaps of organic semiconductor materials. *Opt. Mater.* **2016**, *58*, 51–60. [CrossRef]
63. García, M.; Carfumán, K.; Díaz, C.; Garrido, C.; Osorio-Román, I.; Aguirre, M.J.; Isaacs, M. Multimetallic porphyrins/polyoxotungstate-modified electrodes by the layer-by-layer method: Electrochemical, spectroscopic and morphological characterization. *Electrochim. Acta* **2012**, *80*, 390–398. [CrossRef]
64. Crespilho, F.N.; Zucolotto, V.; Siqueira, J.R., Jr.; Carvalho, A.J.F.; Nart, F.C.; Oliveira, O.N., Jr. Using electrochemical data to obtain energy diagrams for layer-by-layer films from metallic phthalocyanines. *Int. J. Electrochem. Sci.* **2006**, *1*, 151–159. [CrossRef]
65. Zhang, X.; Li, X.-D.; Ma, L.-X.; Zhang, B. Electronic and electrochemical properties as well as flowerlike supramolecular assemblies of fulleropyrrolidines bearing ester substituents with different alkyl-chain lengths. *RSC Adv.* **2014**, *4*, 60342–60348. [CrossRef]
66. Guido, C.; Cortona, P.; Mennucci, B.; Adamo, C. On the Metric of Charge Transfer Molecular Excitations: A Simple Chemical Descriptor. *J. Chem. Theory Comput.* **2013**, *9*, 3118–3126. [CrossRef] [PubMed]
67. Schmidt-Mende, L.; Fechtenkötter, A.; Müllen, K.; Moons, E.; Friend, R.H.; MacKenzie, J.D. Self-organized discotic liquid crystals for high-efficiency organic photovoltaics. *Science* **2001**, *293*, 1119–1122. [CrossRef] [PubMed]
68. Schmidt-Mende, L.; Fechtenkötter, A.; Müllen, K.; Friend, R.H.; MacKenzie, J.D. Efficient organic photovoltaics from soluble discotic liquid-crystalline materials. *Phys. E.* **2002**, *14*, 263–267. [CrossRef]
69. Hesse, H.C.; Weickert, J.; Al-Hussein, M.; Dössel, L.; Feng, X.; Müllen, K.; Schmidt-Mende, L. Discotic materials for organic solar cells: Effects of chemical structure on assembly and performance. *Sol. Energy Mater. Sol. Cells* **2010**, *94*, 560–567. [CrossRef]

Disclaimer/Publisher's Note: The statements, opinions and data contained in all publications are solely those of the individual author(s) and contributor(s) and not of MDPI and/or the editor(s). MDPI and/or the editor(s) disclaim responsibility for any injury to people or property resulting from any ideas, methods, instructions or products referred to in the content.